

Experimental evidence of crystal-field, Zeeman-splitting, and spin-phonon excitations in the quantum supersolid $\text{Na}_2\text{BaCo}(\text{PO}_4)_2$

Ghulam Hussain ^{1,*}, Jianbo Zhang ^{2,*}, Man Zhang ¹, Lalit Yadav,³ Yang Ding,² Changcheng Zheng,¹ Sara Haravifard ^{3,4} and Xiawa Wang^{1,†}

¹*Division of Natural and Applied Sciences, Duke Kunshan University, Kunshan, Jiangsu 215316, China*

²*Center for High-Pressure Science and Technology Advanced Research, Beijing 100094, China*

³*Department of Physics, Duke University, Durham, North Carolina 27708, USA*

⁴*Department of Mechanical Engineering and Materials Science, Duke University, Durham, North Carolina 27708, USA*



(Received 18 November 2024; revised 19 February 2025; accepted 26 March 2025; published 17 April 2025)

Drawing inspiration from the recent breakthroughs in the $\text{Na}_2\text{BaCo}(\text{PO}_4)_2$ quantum magnet, renowned for its spin supersolidity phase and its potential for solid-state cooling applications, our study delves into the interplay among lattice, spin, and orbital degrees of freedom within this compound. Using temperature-, field-, and pressure-dependent Raman scattering techniques, we present experimental evidence revealing crystal-electric-field (CEF) excitations, alongside the interplay of CEF-phonon interactions. We performed density functional theory calculations for the phonon frequencies and compared them with the experimentally observed modes. In addition, our experiments elucidated electronic transitions from $j_{1/2}$ to $j_{3/2}$ and from $j_{1/2}$ to $j_{5/2}$, with energy levels closely aligned with theoretical predictions based on point-charge models. Moreover, the application of a magnetic field and pressure revealed Zeeman splittings characterized by Landé- g factors as well as the CEF-phonon resonances. The anomalous shift in the coupled peak at low temperatures originated from the hybridization of CEF and phonon excitations due to their close energy proximity and shared symmetry. These findings constitute a significant step towards unraveling the fundamental properties of this exotic quantum material for future research in fundamental physics or engineering application.

DOI: [10.1103/PhysRevB.111.155129](https://doi.org/10.1103/PhysRevB.111.155129)

I. INTRODUCTION

In contemporary condensed matter physics, a significant endeavor revolves around identifying an isotropic and geometrically frustrated system capable of hosting an ideal two-dimensional (2D) triangular lattice. This system should be characterized by effective spin-1/2 local moments, devoid of structural imperfections or inherent chemical disorder [1–7]. $\text{Na}_2\text{BaCo}(\text{PO}_4)_2$ (NBCP) has emerged as an interesting material due to its nearly perfect triangular lattice structure devoid of inherent chemical disorder or site mixing [8]. From previous experimental results, the material not only unveiled emergent quantum phenomena, including spin-orbit coupling (SOC), crystalline-field effects, topological order, and fractionalized excitations deviating from conventional spin-wave behaviors [9–13], but also offered promising avenues for next-generation advancements in energy storage, conversion, magneto-caloric effects (MCE), and novel computational paradigms [14,15]. Experimental evidence supports NBCP as a host for a spin supersolid phase [14,16], with Co^{2+} ions exhibiting effective spin-1/2 characteristics. Moreover, NBCP displays a broad continuum observed in inelastic neutron scattering, attributed to spinon excitations, alongside antiferromagnetic exchange without long-range

ordering down to 0.05 K [8,12]. Subsequent investigations via ultralow-temperature specific heat and thermal conductivity measurements indicated an antiferromagnetic phase transition occurring at the Néel temperature (T_N) of 148 mK [17]. Recent findings from muon spin relaxation (μSR) and nuclear magnetic resonance experiments suggest magnonlike magnetic excitations transitioning to spinons at the critical field $\mu_0 H_C = 1.65$ T [18]. Moreover, Gao *et al.* observed persistent spin fluctuations until low temperatures and proposed a spin supersolid state with Kosterlitz-Thouless-Berezinskii (BKT) fluctuations of the U(1) phase [16].

In compounds containing transition-metal ions, the interplay between spin, lattice, and electronic degrees of freedom in magnetic materials can lead to new phenomena. For example, in ferromagnetic $\text{Co}[\text{N}(\text{CN})_2]_2$, strong electron-phonon coupling is evident from a magnetic-field-driven avoided crossing of low-lying Co^{2+} excitations with two ligand phonons [19]. In some materials, the hybridization of CEF and phonons can generate significant phonon magnetic moments, such as in CoTiO_3 [20]. On the other hand, phonon anomalies observed in the Raman data can sometimes give important insight into the magnetic entropy changes as provided in the material $\text{Co}_3\text{V}_2\text{O}_8$ [21]. As a material exhibiting a large magneto-caloric effect [14], our data can provide important insight in developing $\text{Na}_2\text{BaCo}(\text{PO}_4)_2$ as a promising functional material in solid-state cooling.

In this study, we present a comprehensive analysis of NBCP, employing temperature-, polarization-,

*These authors contributed equally to this work.

†Contact author: xiawa.wang@dukekunshan.edu.cn

magnetic-field-, and pressure-dependent Raman spectroscopy down to 7 K, with magnetic field up to 8 T and pressure up to 2.18 GPa. Our investigations reveal all the primary phonons and crystal-field excitations (CEF) with their energies corroborated through density functional theory (DFT) and point-charge model calculations. In addition, we discovered peak splittings with the application of magnetic field and pressure, indicating different mechanisms that originated from the Zeeman effect, CEF-phonon coupling, and anisotropy of the Landé- g factor. This work constitutes direct experimental evidence of the spin-lattice interplays in NBCP under applied pressure and magnetic field, thereby opening different avenues for exploring its exotic properties and facilitating further research in this material.

II. EXPERIMENTAL METHOD

We synthesized high-quality $\text{Na}_2\text{BaCo}(\text{PO}_4)_2$ single crystals using the conventional flux method [8,22]. Initially, polycrystalline NBCP samples were prepared via solid-state reaction. The precursor powders, including Na_2CO_3 (99%, Alfa Aesar), BaCO_3 (99.99%, Adamas), CoO (99%, Alfa Aesar), and $(\text{NH}_4)_2\text{HPO}_4$ (99.5%, Sigma-Aldrich), were thoroughly mixed using an agate mortar and pestle. The mixture was then annealed in air at 700 °C for 24 hours. Subsequently, the dried powders were combined with NaCl flux (in a molar ratio of 1:5) and placed in a platinum crucible covered with a lid inside a box-type furnace. The crucible was heated to 950 °C, held for 2 hours for homogenization, and slowly cooled to 750 °C at a rate of 2 °C/hour. Pink crystals were obtained, washed in water, and manually separated from the bulk, resulting in typical dimensions of $2 \times 1 \times 0.3 \text{ mm}^3$, as depicted in Fig. 1(b) (inset). Raman spectroscopy was performed using linearly polarized lasers with wavelengths of 488 and 532 nm, yielding a spot size of approximately 5 μm on the sample employing a grating of 1800 g/mm. Spectra were collected in parallel (XX) and crossed (XY) polarization configurations, with phonon vibrational anisotropy explored by rotating the laser-polarization direction. For later discussions, we used the experimental values from the 488 nm laser excitations. Peak positions were extracted by fitting the Raman spectra with Lorentzian oscillators with the uncertainty from the fitting reported as the error bar. For temperature- and field-dependent measurements, single crystals were placed in a helium closed-cycle cryostat, allowing temperature variation between 7 and 300 K. Crystal orientations in the ab and ac planes were accessed by placing samples on the cold stage in two directions. Temperature- and field-dependent spectra were recorded in both planes, with an exposure time of 90 s and a laser power reaching the cryostat's optical window of approximately 8 mW for each spectrum. The calculation of zone-centered phonons was done using the plane-wave approach implemented in QUANTUM ESPRESSO [23,24]. All the calculations were carried out using optimized norm-conserving Vanderbilt pseudopotentials. The plane-wave cutoff energy was set to 120 Ry. Dynamical matrix and eigenvectors were determined using density functional perturbation theory. The numerical integration over the Brillouin zone were done with a 191 k -point mesh in the Monkhorst-Pack grid. In our calculations, we use fully relaxed

ionic positions with experimental lattice parameters given in Ref. [8].

III. RESULTS AND DISCUSSIONS

A. Phonon excitations

$\text{Na}_2\text{BaCo}(\text{PO}_4)_2$ crystallizes in a trigonal structure with lattice parameters $\alpha = \beta = 90^\circ$, $\gamma = 120^\circ$, and lattice constants $a = b = 5.313 \text{ \AA}$, $c = 7.008 \text{ \AA}$ in space group $P\bar{3}m1$ (No. 164) [8] and point group D_{3d}^3 ($\bar{3}m1$ in Hermann-Mauguin notation) as depicted in Figs. 1(a) and 1(b). The triangular layer of magnetic CoO_6 octahedra resides in the ab plane with each Co^{2+} ion coordinated to six oxygen atoms. With a layered AA stacking along the c axis, the Co^{2+} ions ideally form an effective two-dimensional (2D) triangular lattice to be free of chemical disorders or structural distortions. The polarization-dependent Raman spectra at room temperature under ambient pressure are depicted in Fig. 1(c). The bulk unit cell comprises a total of 14 atoms, resulting in 42 normal phonon modes at the Γ point. The Co and Ba atoms occupy C_{3v} sites in each unit cell, while the remaining 6 O atoms binding to Co atoms occupy the C_s sites. The vibrational modes at the Γ point can be categorized into $\Gamma(D_{3d}^3) = 5A_{1g} + 7A_{2u} + 6E_g + 8E_u + A_{2g} + A_{1u}$. Among these vibrational modes, 11 are Raman active modes corresponding to the nondegenerate A_{1g} symmetry modes and the doubly degenerate E_g symmetry modes. Moreover, the energy values between experimental values and *ab initio* computations by QUANTUM ESPRESSO matched very well, as seen in Table I [8,25–28]. The symmetry analysis reveals that the E_g mode can be observed in both cross and parallel configurations, while the A_{1g} mode is visible only in the parallel polarization configuration as verified by the experimental observation in Figs. S1 and S2 in the Supplemental Material [29]. The Raman tensors of the two modes are given as shown in Eqs. (1)–(3) [30–32].

The intensity of a Raman mode, denoted as I , is proportional to $|e_i \cdot R \cdot e_s|^2$, where R is the Raman tensor of the phonon mode, and e_i and e_s are the unitary polarization vectors of the incident and scattered light, respectively [33–35]. For the A_{1g} mode, by substituting the Raman tensor, we can obtain the mode's different responses to polarization, as shown in Eqs. (4) and (5). Under the parallel configuration where $\gamma = \theta$, the intensity $I(A_{1g})$ is proportional to $|a|^2$, resulting in a circular polarization profile. Conversely, under the experimental cross configuration where $\gamma = \theta + 90^\circ$, $I(A_{1g}) = 0$, indicating that the mode is nonvisible as confirmed by the experiment. Similarly, for the E_g mode, we have $I(E_g) \propto |c|^2$ so that the polarization profile is circular and visible for both polarizations,

$$I(A_{1g}) \propto \left| (\cos \gamma, \sin \gamma, 0) \cdot \begin{pmatrix} a & \cdot & \cdot \\ \cdot & a & \cdot \\ \cdot & \cdot & b \end{pmatrix} \cdot \begin{pmatrix} \cos \theta \\ \sin \theta \\ 0 \end{pmatrix} \right|^2, \quad (1)$$

$$I(A_{1g}) \propto |a|^2 \cos^2(\gamma - \theta), \quad (2)$$

$$R(A_{1g}) = \begin{pmatrix} a & \cdot & \cdot \\ \cdot & a & \cdot \\ \cdot & \cdot & b \end{pmatrix}, \quad (3)$$

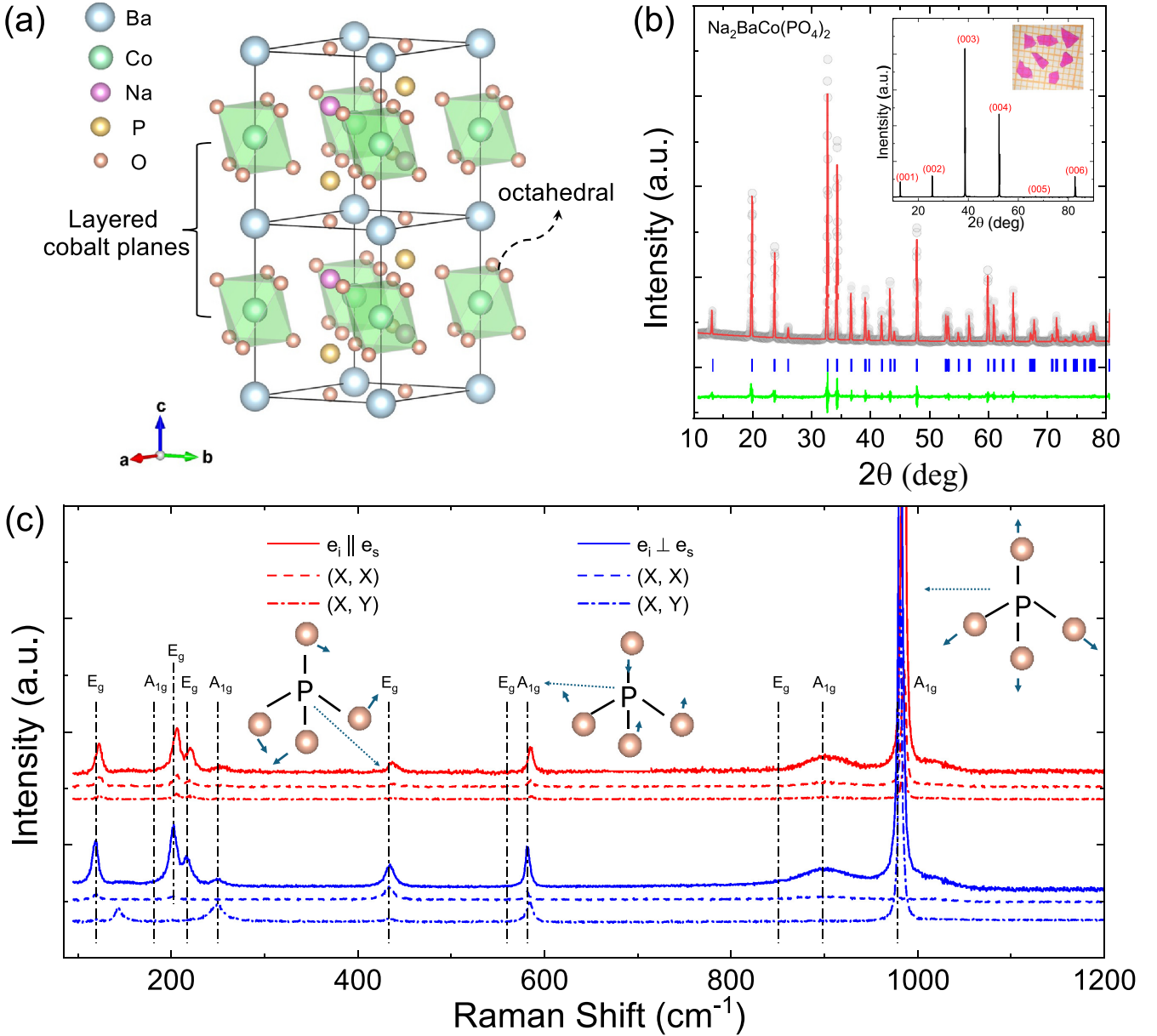


FIG. 1. (a) NBCP crystal structure. (b) The room-temperature powder XRD pattern and inset showing the single-crystal XRD, indicating the well-grown (001) surface with a photograph image. (c) The incident light polarization e_i is aligned along the x direction, while the scattered light polarization e_s can be either parallel (x direction) or perpendicular (y direction) to e_i . Spectra were collected in parallel (XX) and crossed (XY) polarization configurations on the ab and ac planes of the NBCP single crystals at room temperature.

$$R(E_g) = \begin{pmatrix} c & \cdot & \cdot \\ \cdot & -c & d \\ \cdot & d & \cdot \end{pmatrix}, \quad (4)$$

$$R(E_g) = \begin{pmatrix} \cdot & -c & -d \\ -c & \cdot & \cdot \\ -d & \cdot & \cdot \end{pmatrix}. \quad (5)$$

B. Crystal-field excitations

We characterized the temperature-dependent (7–300 K) Raman spectra of NBCP with the whole set of data given in the Supplemental Material, Figs. S3(a) and S3(b) [29]. The spectra collected using 488 and 532 nm laser

excitations exhibited similar spectra, except the peak of 526 cm^{-1} , which is only visible in the 488 nm laser excitation possibly due to a weak intensity, as shown in Fig. S3(c) in the Supplemental Material [29]. As the temperature decreased, the phonon modes shifted to higher frequencies, as illustrated in Fig. S3(d) in the Supplemental Material [29]. Two soft phonons at 867 and 871 cm^{-1} exhibited decreasing energies as the temperature decreases, as shown in Fig. 2(g). Below 130 K at ambient pressure, an additional five peaks emerged. These peaks appeared at 309 cm^{-1} (38 meV), 346 cm^{-1} (42 meV), 862 cm^{-1} (107 meV), 900 cm^{-1} (112 meV), and 1036 cm^{-1} (128 meV) demonstrating strong temperature-dependent intensities, weak polarization dependence, and linewidth softening as the temperature decreased. The

TABLE I. A comparison of DFT calculated phonon frequencies and experimentally observed values with two different laser excitations (488 and 532 nm).

Mode	Calc. (cm ⁻¹)	Expt. (488 nm)(cm ⁻¹)	Expt. (532 nm)(cm ⁻¹)	Mode	Calc. (cm ⁻¹)
$E_g(\text{R})$	120.1	120	117	$E_u(\text{IR})$	37
$A_{1g}(\text{R})$	186.1	166	164	$E_u(\text{IR})$	111.8
$E_g(\text{R})$	201.8	201	199	$A_{2g}(-)$	155.0
$E_g(\text{R})$	236	224	220	$A_{2u}(\text{IR})$	155.6
$A_{1g}(\text{R})$	270	254	251	$E_u(\text{IR})$	195.7
		309(38 meV)	309	$A_{1u}(-)$	197.5
		346(42 meV)	342	$A_{2u}(\text{IR})$	214.1
$E_g(\text{R})$	425	430	429	$E_u(\text{IR})$	228.2
$E_g(\text{R})$	562.7	526	...	$A_u(\text{IR})$	239.7
$A_{1g}(\text{R})$	567.9	580	577	$A_{2u}(\text{IR})$	279.8
		862 (107 meV)	858	$E_u(\text{IR})$	404.1
$E_g(\text{R})$	868.2	867	863	$A_{2u}(\text{IR})$	533.8
$A_{1g}(\text{R})$	886.5	871	870	$E_u(\text{IR})$	563.6
		900 (112 meV)	900	$A_{2u}(\text{IR})$	873.5
$A_{1g}(\text{R})$	1021	977	980	$E_u(\text{IR})$	887.2
		1036 (128 meV)	1033	$A_{2u}(\text{IR})$	980.5

extracted line width and Raman intensity data in the 7–140 K temperature range can be seen in the Supplemental Material, Figs. S4(a)–S4(d) [29]. The observed energy values can be roughly grouped into two transition levels: two peaks appeared in the range of 300 cm⁻¹, around 40 meV, and another three between 800 and 1100 cm⁻¹, in the range of 110 meV. However, the two lower-energy peaks shown in Figs. 2(b) and 2(c) persisted roughly to 130 K and demonstrated opposite shifting directions as phonons, as shown in Fig. 2(d). Moreover, the two higher-energy peaks with energies at 107 meV (862 cm⁻¹) and 112 meV (900 cm⁻¹) showed up as one broad peak persisting all the way to room temperature, as shown in Fig. 2(e). Upon deconvolution, we discovered four peaks inside, which were the two phonon peaks of E_g at 867 cm⁻¹ (107 meV), A_{1g} at 871 cm⁻¹ (108 meV), together with the two new peaks at 862 cm⁻¹ (107 meV) and 900 cm⁻¹ (112 meV), as shown in Fig. 2(f) and in the Supplemental Material, Figs. S1(a) and S1(b) [29]. Figure 2(g) showed the anomalous shifting directions for these peaks, suggesting potential hybridization or couplings that will be discussed later. A third newly emerged peak at 1036 cm⁻¹ (128 meV) was further away from any phonon peaks and appeared as an independent one below 130 K.

We attribute these additional peaks to crystal-field excitations in the presence of spin-orbit coupling and small trigonal distortion and further verified our conclusion by the point-charge model computation and theoretical values reported in the literature. In Na₂BaCo(PO₄)₂, the cobalt ion exists in the Co²⁺ state with an electronic configuration of 3d⁷. Figure 2(a) illustrates the energy diagram for the cobalt ion situated within an octahedral crystal field under the influence of spin-orbit coupling. Expressed in term symbols, the electronic ground state for the Co²⁺ ion is ⁴F with $L = 3$ and $S = 3/2$, resulting in $2L + 1 = 7$ initially degenerate levels for the free ion. Subjecting to the octahedral field, the energy levels split into the T_{1g} mode (subject to Γ_4 symmetry), the T_{2g} mode (Γ_5), and the higher A_{2g} mode (Γ_2). Spin-orbit coupling further splits the energy levels into a $j = 1/2$ doublet (subject to

Γ_6 symmetry), a $j = 3/2$ quartet (Γ_8), and a $j = 5/2$ sextet with four transforming according to Γ_7 and the others according to Γ_8 symmetries. A group theory analysis revealed the Raman activity of these sublevel transitions between T_{1g} ground term sublevels, as shown in the Supplemental Material, Table S1 [29]. The experimental results also agreed with a recent theoretical paper on the computation of NBCP's Raman spectroscopy with a small negative trigonal distortion so that ligands are pushed closer together in the xy plane while being pulled farther apart along the z axis, resulting in a weak $j = 5/2$ peak plus two stronger $j = 5/2$ peaks at higher wave numbers [25]. In the low-temperature measurement without magnetic field, the Hamiltonian can be represented according to Eq. (6),

$$H = H_{\text{Crys}} + H_{\text{SOC}} = \sum_{n,m} B_n^m O_n^m + \lambda_{\text{SO}} S \cdot L. \quad (6)$$

Here, H_{Crys} represents the crystal-field contribution, which can further be expanded into a series of spherical harmonics where B_n^m are the CEF multiplicative factors related to the strength of the crystal field and O_n^m belong to the Stevens' operators. The spin-orbit coupling H_{SOC} can be expressed as the dot product of the operators with a spin-orbit-coupling constant λ_{SO} . By directly constructing a point-charge model based on the NBCP structure, the calculations were performed using the open-source package PYCRYSTALFIELD [36]. Table II compares our measured energy levels with point-charge computation and the theoretical values done by density functional theory [37]. The computed CEF constants were $B_2^0 = -1.53$ meV, $B_4^0 = 0.43$ meV, and $B_4^3 = 12.28$ meV, with the spin-orbit-coupling constant $\lambda_{\text{SO}} = -22$ meV from the literature [28].

The peak positions are in excellent agreement with the transition energies from the ground state $j = 1/2$ to the excited states $j = 3/2$ and $j = 5/2$. The two lower-energy peaks arose from the smaller energy gap between $j = 1/2$ and $j = 3/2$, while the three higher-energy ones correspond to the transition from $j = 1/2$ to $j = 5/2$. These transitions

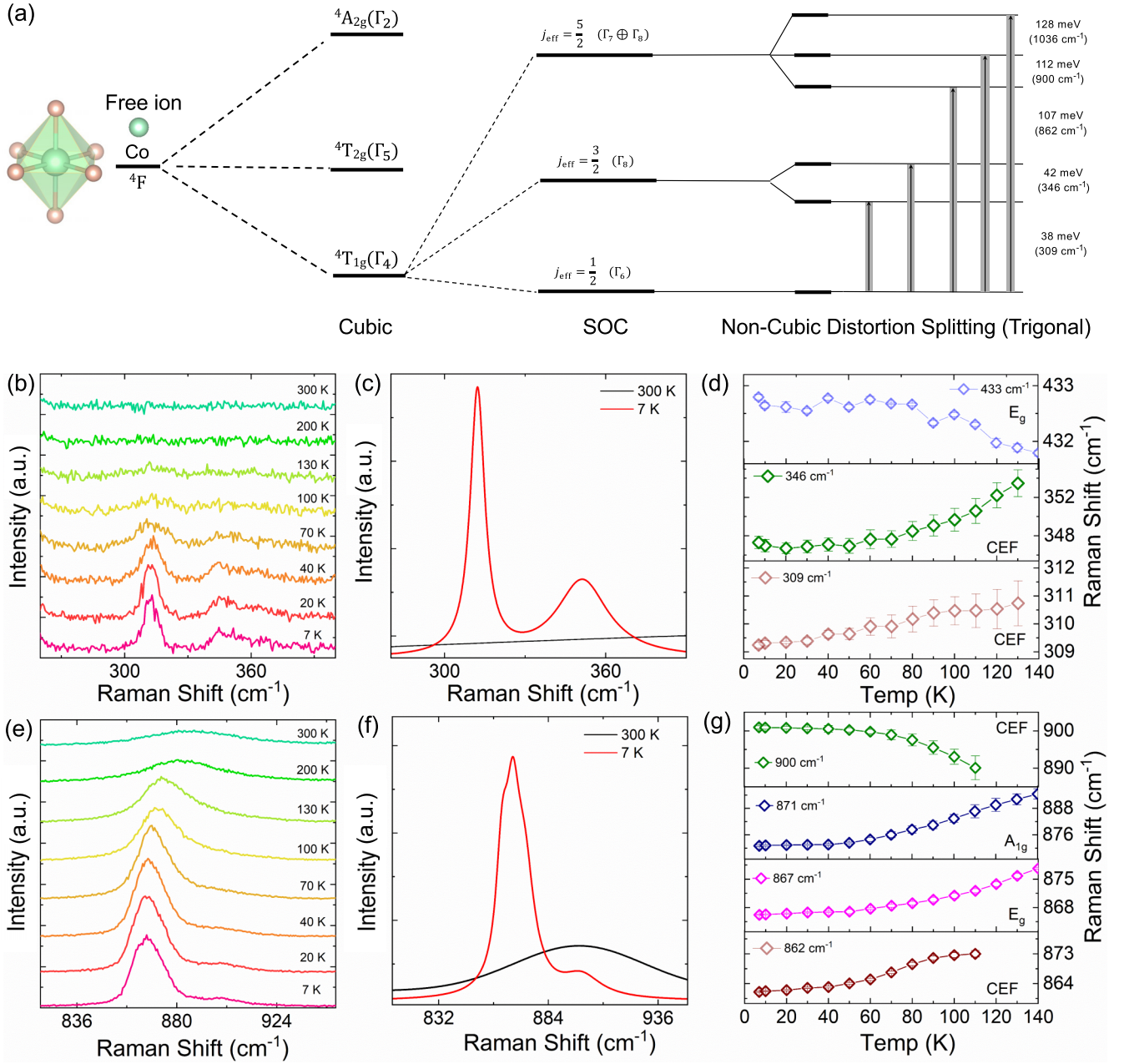


FIG. 2. (a) The energy levels of the ground $4F$ Co^{2+} split by the crystal field in the presence of SOC and trigonal distortion. (b) The temperature-dependent CEF excitation peaks around (300 cm^{-1}) 40 meV. (c) A comparison of low- and room-temperature Raman spectra of the 40 meV CEF peaks. (d) Peak position evolution as a function of temperature for phonon and 40 meV CEF peaks. (e) The temperature-dependent CEF excitation peaks around $(800\text{--}1100 \text{ cm}^{-1})$ 110 meV. (f) A comparison of low- and room-temperature Raman spectra for the 110 meV CEF peaks (two lower peaks). (g) Peak position evolution as a function of temperature for the two lower 110 meV CEF peaks and adjacent phonon peaks.

TABLE II. Comparison of experimental and calculated CEF levels.

Experimental	Point-charge calculation	DFT from the literature [25,37]
38.3 meV (309 cm^{-1})	37.3 meV	40.7 meV
42.4 meV (346 cm^{-1})	43.2 meV	45.6 meV
106.9 meV (862 cm^{-1})	104.2 meV	112.4 meV
111.6 meV (900 cm^{-1})	113.4 meV	113.6 meV
128.4 meV (1036 cm^{-1})	133.4 meV	128.3 meV

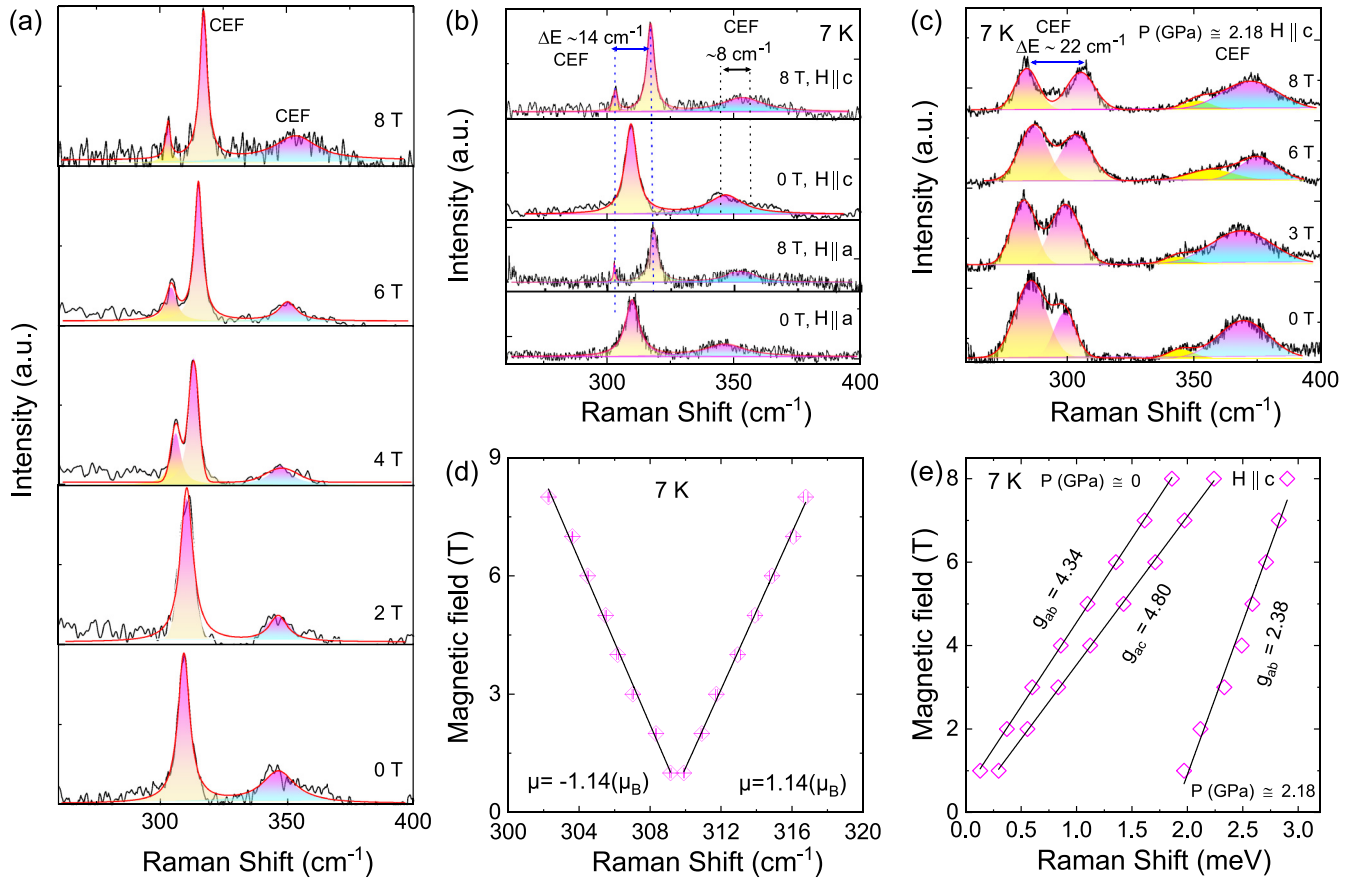


FIG. 3. (a) Zeeman splitting of 34 meV peak at lower temperature (7 K) with increasing magnetic field perpendicular to the *ab* plane. (b) The comparison of the spectra with and without magnetic field in different orientations. (c) Under $P = 2.18$ GPa applied pressure, the 40 meV peaks evolves as a function of magnetic field. (d) The Zeeman splitting valley showing the peak shift as a function of the field. (e) The slope fit yielded g values obtained from the energy shift as a function of the applied magnetic field.

involved a change in the angular momentum quantum number, leading to a nonzero transition moment that renders them observable in Raman spectroscopy. Our results are also consistent with another recent report for this material, indicating the presence of unconventional magnetism driven by spin-orbit coupling, electronic correlations, and CEF excitations [25].

C. Zeeman splitting

In crystal-field theory, metal-ligand interactions are typically considered to be solely electrostatic, suggesting field-independent Raman excitations at low temperatures. However, the behavior of the CEF peaks in NBCP was more complex, showing splitting and strong dependence with applied magnetic field and pressure. The complete dataset is provided in Figs. S5(a) and S5(b) in the Supplemental Material [29], with zoomed views of the CEF excitations shown in the side panels. For the lower-energy peaks that we designated as transition from $j = 1/2$ and $j = 3/2$, the two peaks exhibited shifts to higher frequencies at a rate of ~ 1.7 cm^{-1}/T and ~ 1.0 cm^{-1}/T , respectively. Moreover, when the field strength increased beyond 3 T, a third peak moving in the opposite direction appeared, which we attributed to Zeeman splitting, as illustrated in Fig. 3(a). To validate our

conclusion, we applied a magnetic field in both the parallel and perpendicular directions. The 38 meV (309 cm^{-1}) peak showed up $\Delta E \sim 14$ cm^{-1} in response to the 8 T applied field in both the $H \parallel c$ and $H \parallel a$ directions, as shown in Fig. 3(b). When a pressure of $P = 2.18$ GPa was applied, the peak splitting width increased from $\Delta E \sim 14$ cm^{-1} to $\Delta E \sim 22$ cm^{-1} , as shown in Fig. 3(c), signifying that the energy levels are more distinct under pressure. It is noteworthy that the nonsplit peak at 42 meV (346 cm^{-1}) also started to show splitting under high pressure once a magnetic field was applied. This was potentially due to the impact of pressure that makes the Zeeman effect more detectable. However, as the 42 meV (346 cm^{-1}) peak split was very weak, we extracted most of the information from the 38 meV (309 cm^{-1}) peak instead.

Typically, the interaction between an external magnetic field and the magnetic dipole moment associated with the total angular momentum of an ion leads to Zeeman splitting. We used the energy difference between the split modes to calculate the effective magnetic moment (μ_{eff}) and the associated g factor using the equation $\Delta E = 2g\mu_B B$, where ΔE represents the peak-peak splitting for a given applied magnetic field B , and μ_B denotes the Bohr magneton. The extracted data as a function of magnetic field with a linear fitting are shown in Fig. 3(d). A g factor of $g_{\perp} = 4.34$ and $g_{\parallel} = 4.80$

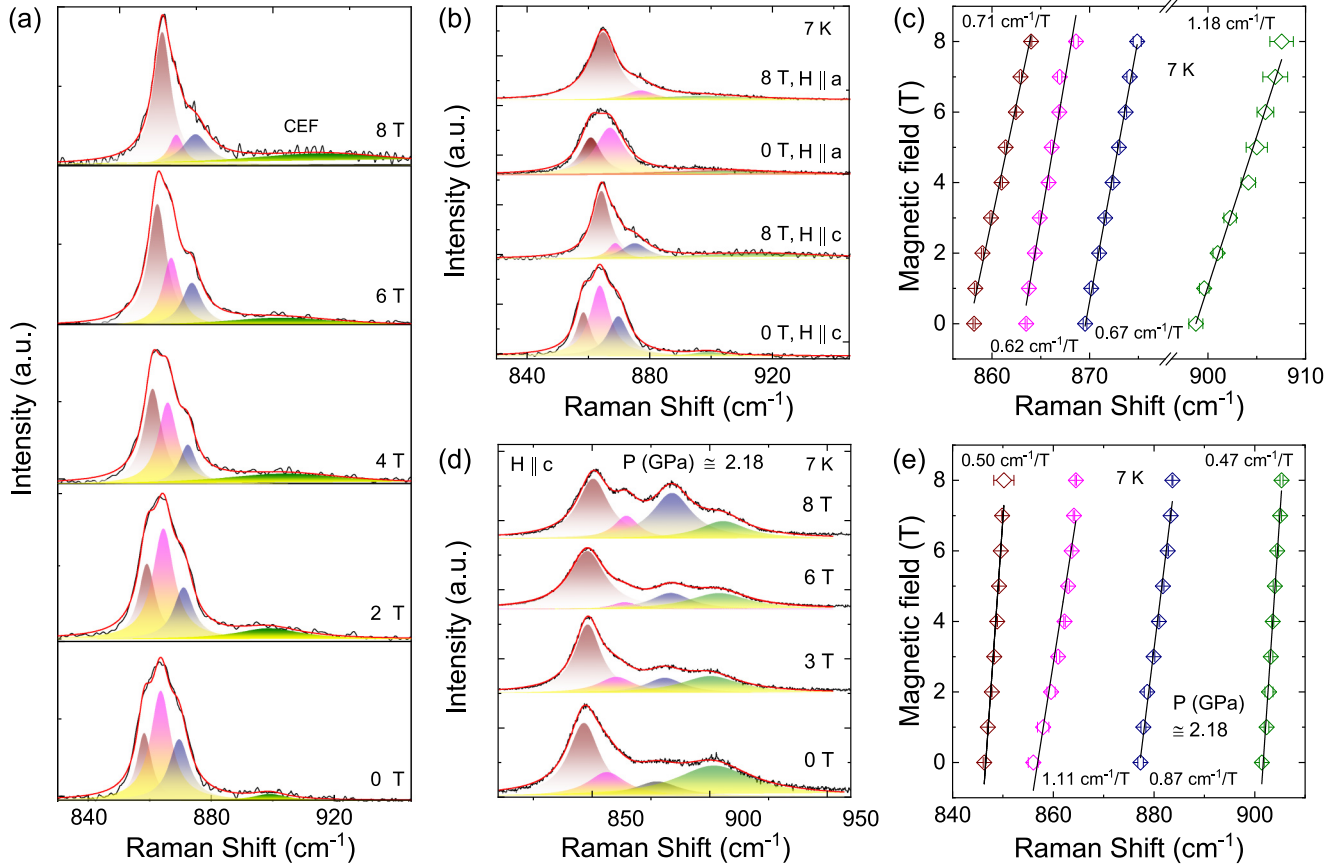


FIG. 4. (a) Deconvolution of Raman spectra 800–960 cm^{-1} . (b) The peak intensity in response to the applied field along different crystal's axis. (c) Low-temperature ($T = 7$ K) Raman spectra of NBCP at $P = 2.18$ GPa with an applied magnetic field. Four distinct peaks showed up. (d) Linear fits of the peak shifts as a function of field strength at ambient pressure. (e) Linear fits of the peak shifts as a function of field strength at 2.18 GPa pressure.

values and the effective magnetic moment $\mu_{\text{eff}} \approx 1.14 \mu_B$ can be extracted as seen in Figs. 3(d) and 3(e), which is in excellent agreement with the electron spin resonance (ESR) experiment values of $g_{\perp} = 4.22$ and $g_{\parallel} = 4.81$ [8,37]. For $\text{Na}_2\text{BaCo}(\text{PO}_4)_2$, the g factor was theoretically predicted to be anisotropic because of the small trigonal distortion [16,38]. It is plausible that the different transition observations CEF peaks were caused by the anisotropy of the g factor, resulting from different angular momenta change to show up under a magnetic field [8,37,39].

D. CEF-phonon coupling

The higher-energy Raman mode, centered around 110 meV, responded to the magnetic field in a markedly different way. According to the point-charge model, there are three transitions arising from $j = 1/2$ to $j = 5/2$ located at 862 cm^{-1} (107 meV), 900 cm^{-1} (112 meV), and 1036 cm^{-1} (128 meV). However, within a similar energy range, two phonons, i.e., the E_g mode at 867 cm^{-1} (108 meV) and the A_{1g} mode at 871 cm^{-1} (108 meV), are also present. Extracted linewidth and intensity for the CEF, E_g , and A_{1g} modes in NBCP under magnetic fields of up to 8 T, can be seen in Figs. S6(a)–S6(d) [29]. The two phonons come from the PO_4 tetrahedron's symmetric

stretching and asymmetric stretching vibration modes for the corresponding phosphate with the glaserite-type phase [40–42]. This suggests a potential coupling between the CEF and phonon modes contributing to this peak. Typically, the electronic excitations that are close to phonons can come from the CEF and the magnetic ions' spin-orbit effects, where the spin and orbital degree of freedom can strongly interact responding to a magnetic field [43,44]. To investigate this hypothesis, we deconvolved the peak (by multiple peak fitting) into four contributors in the spectral range 800–980 cm^{-1} , among which two are CEF peaks and two are phonon peaks, and analyzed their frequency dependence on the field strength as shown in Figs. 4(a) and 4(b). In the absence of a magnetic field, the lowest CEF peak at 107 meV (862 cm^{-1}) showed the smallest intensity buried by the two phonons. When field strength increased, the CEF displayed strong intensity up to 8 T along both the ab and ac planes. Furthermore, the linewidth and intensity of the CEF mode at 862 cm^{-1} (107 meV) exhibited stronger field dependence compared to the 900 cm^{-1} (112 meV) CEF mode, as shown in Fig. 4(a) and the Supplemental Material, Figs. S6(a)–S6(d) [29]. With continuously increased magnetic field, the E_g mode intensity greatly reduced at the expense of the 862 cm^{-1} (107 meV) CEF peak, while the total peak intensity remained approximately conserved potentially due

to the hybridization of the CEF mode and phonon. The CEF-phonon coupling can lead to resonances observed in many rare-earth compounds as reported for Ce_2O_3 [45], Eu_2O_3 , and Yb_2O_3 [46,47], etc. Moreover, closely related examples of Co-based materials include $\text{Na}_2\text{BaCo}(\text{PO}_4)_2$ [25], $\text{Na}_3\text{Co}_2\text{SbO}_6$ [48], $\text{Na}_2\text{Co}_2\text{TeO}_6$ [49], $\text{BaCo}_2(\text{AsO}_4)_2$ [50], and CoX_2 ($X = \text{Cl, Br, I}$) [51]. When CEF-phonon coupling was observed, phonon softening is often a strong indicator and sometimes large phonon magnetic moments can be observed in magneto-Raman spectra [43,52,53]. Based on the theory developed by Thalmeier and Fulde [54,55], energy proximity and shared symmetries between the phonon and CEF electronic excitations are necessary criteria for such resonance to occur. In NBCP, the phonons' proximity to the resonance was observed at roughly the same position, 107 meV (867 cm^{-1}) E_g and A_{1g} at 108 meV (871 cm^{-1}) mode, close to the CEF mode at 107 meV (862 cm^{-1}). Both phonon modes exhibited anomalous softening with decreasing temperature, as shown in Fig. 2(g), consistent with observations in materials with similar coupling. The irreducible representation of the local distortion by the phonon at the cobalt site can be obtained by the subduction from the $O(3)$ of the point group [56,57]. The symmetry of the CEF-phonon coupling states can be obtained by direct product of the CEF and the phonon distortion at the ion site, as shown in the Supplemental Material, Table S1 [29]. Therefore, we can confidently say that both conditions for the Thalmeier-Fulde resonance were satisfied: the energetic proximity as well as the shared symmetries between the two types of excitations.

When applying the field in different crystallographic directions, there were obvious differences for this coupling behavior, as shown in Fig. 4(b). First, only two peaks can be deconvolved because the A_{1g} phonon mode was only visible in one polarization. However, CEF-phonon energy and intensity trade-offs can be seen regardless of the field direction. To extract more quantitative information about the interaction between Co^{2+} electronic excitations and phonons, we applied a coupled oscillator equation to extract the coupling constants, where the perturbed energy levels of the two coupled modes are described in Eq. (7) [19,45]:

$$\omega_{1,2} = \frac{\omega_{\text{ph}} + \omega^*}{2} \pm \sqrt{\left(\frac{\omega_{\text{ph}} - \omega^*}{2}\right)^2 + \lambda^2}. \quad (7)$$

Here, ω_{ph} and ω^* are the phonon and Co^{2+} electronic excitation frequencies, and λ is the coupling constant. We estimate the electron-phonon interaction energy to be approximately 1.40, 1.61, 1.49, and 0.85 cm^{-1} for the 862, 867, 871, and 900 cm^{-1} modes, respectively. Taking into account the field dependence of electronic excitation, the best fit to the magneto-Raman data was obtained using these coupling constants, as shown in Fig. 4(c). A notable point is that the coupled phonons exhibited strong magnetic field dependence, while all other phonons' response are largely field independent, as shown in the Supplemental Material, Fig. S7 [29]. The large magnetic moments of the coupled phonons agreed with similar materials [20].

An applied pressure can easily separate the contributors to this peak, as seen in Fig. 4(d), and the evolution of the line width and Raman intensity data for $P = 2.18 \text{ GPa}$ under magnetic fields ranging from 0 to 8 T can be seen in Fig. S8 in the Supplemental Material [29]. When a pressure of 2.18 GPa was applied, the peaks broadened and were separated even without magnetic field. The change of the Raman spectra can possibly be explained by the direction of the trigonal distortion. With a pressure applied in the perpendicular direction, the ligands were pushed closer in the z axis, resulting in a positive distortion instead of the negative one that was intrinsic to a nonpressured sample. A positive distortion will result in two stronger $j = 5/2$ CEF peaks as can obviously be seen in the blue and green fittings in Fig. 4(c). With a continuously increasing field, the peak separation became more prominent. At the maximum field strength of 8 T, the pressure resolved the peaks and separated them into four distinct contributors. However, a noteworthy point is that CEF-phonon coupling was also present in the high-pressure spectra, but far away from the resonant regime. The peak positions as a function of the applied magnetic field with pressure are shown in Fig. 4(e). Comparing with the nonpressured field-dependence data, the phonon peaks' responsiveness to the magnetic field roughly remained the same level, while the CEFs' responsiveness reduced. This can be explained as a more pronounced impact by the lattice distortion on the particle dynamics so that magnetic contributions were comparatively diminished.

IV. SUMMARY AND CONCLUSION

In summary, we investigated the spin-orbit coupling, crystal-electric-field (CEF) excitations, and CEF-phonon interactions in the exotic supersolid compound $\text{Na}_2\text{BaCo}(\text{PO}_4)_2$ using temperature-, magnetic-field-, and pressure-dependent Raman scattering techniques. We identified and confirmed the symmetries of all primary phonon modes in the material. The temperature-dependent Raman revealed all the energies of CEF excitations from the ground-state to the excited ones, which correlated to the peaks observed at 309 cm^{-1} (38 meV), 346 cm^{-1} (42 meV), 862 cm^{-1} (107 meV), 900 cm^{-1} (112 meV), and 1036 cm^{-1} (128 meV) and in excellent agreement with the point-charge model. Additionally, we observed that the peaks at 38 and 42 meV, which represented the first CEF levels, exhibited field-dependent behavior and Zeeman splitting under magnetic field. The higher-energy CEF modes at 107 and 112 meV created a resonance with two ligand phonons, which can be separated by an applied pressure. This CEF-phonon coupling is shown to be qualitatively described using the two-oscillator model in which the soft phonons are strongly coupled to electronic excitations from CEF transitions. An applied pressure further split the energy levels. The distinct energies associated with spin-orbit coupling, CEF-phonon interactions, and electronic excitations firmly establish NBCP as a promising candidate for further theoretical and experimental investigations into the quantum magnet with nearly ideal triangular lattice. Our results shed light on the intricate interactions within NBCP and offered different avenues for this material for further research in both fundamental physics and practical applications.

ACKNOWLEDGMENTS

We thank Prof. Patrick Lee for helpful discussions. This work is supported by NSFC Young Scientist Program No. 12105124, Gusu Innovation Program No. ZXL2021252, Jiangsu Shuangchuang Prestigious Ph.D. Program, Kunshan Shuangchuang Talent Program No. kssc202202061, and Kunshan Municipal Government Research Fund. Work performed at Duke University is

supported by the U.S. Department of Energy, Office of Science, Office of Basic Energy Sciences, under Award No. DE-SC0023405. Y.D. is supported by the National Key Research and Development Program of China (Grant No. 2022YFA1402301).

G.H., J.Z., C.Z., and X.W. conceived the experiments; G.H., J.Z., X.W., and C.Z. conducted the experiments; G.H., M.Z., and L.Y. analyzed the results; and G.H., Y.D., S.H., and X.W. wrote the paper. All authors reviewed the manuscript.

-
- [1] V. Peri, S. Ilani, P. A. Lee, and G. Refael, Probing quantum spin liquids with a quantum twisting microscope, *Phys. Rev. B* **109**, 035127 (2024).
- [2] N. Tian, Z. Huang, B. G. Jang, S. Guo, Y.-J. Yan, J. Gao, Y. Yu, J. Hwang, C. Tang, M. Wang *et al.*, Dimensionality-driven metal to Mott insulator transition in two-dimensional 1T-TaSe₂, *Natl. Sci. Rev.* **11**, nwad144 (2024).
- [3] R. Sarkar, P. Schlender, V. Grinenko, E. Haeussler, P. J. Baker, T. Doert, and H.-H. Klauss, Quantum spin liquid ground state in the disorder free triangular lattice NaYbS₂, *Phys. Rev. B* **100**, 241116(R) (2019).
- [4] M. M. Bordelon, E. Kenney, C. Liu, T. Hogan, L. Posthuma, M. Kavand, Y. Lyu, M. Sherwin, N. P. Butch, C. Brown, M. J. Graf, L. Balents, and S. D. Wilson, Field-tunable quantum disordered ground state in the triangular-lattice antiferromagnet NaYbO₂, *Nat. Phys.* **15**, 1058 (2019).
- [5] L. Ding, P. Manuel, S. Bachus, F. Grueßler, P. Gegenwart, J. Singleton, R. D. Johnson, H. C. Walker, D. T. Adroja, A. D. Hillier, and A. A. Tsirlin, Gapless spin-liquid state in the structurally disorder-free triangular antiferromagnet NaYbO₂, *Phys. Rev. B* **100**, 144432 (2019).
- [6] A. Chubukov and D. Golosov, Quantum theory of an antiferromagnet on a triangular lattice in a magnetic field, *J. Phys.: Condens. Matter* **3**, 69 (1991).
- [7] O. A. Starykh, Unusual ordered phases of highly frustrated magnets: A review, *Rep. Prog. Phys.* **78**, 052502 (2015).
- [8] R. Zhong, S. Guo, G. Xu, Z. Xu, and R. J. Cava, Strong quantum fluctuations in a quantum spin liquid candidate with a Co-based triangular lattice, *Proc. Natl. Acad. Sci. USA* **116**, 14505 (2019).
- [9] C.-C. Chen, M. van Veenendaal, T. P. Devereaux, and K. Wohlfeld, Fractionalization, entanglement, and separation: Understanding the collective excitations in a spin-orbital chain, *Phys. Rev. B* **91**, 165102 (2015).
- [10] C. Castelnovo, R. Moessner, and S. L. Sondhi, Spin ice, fractionalization, and topological order, *Annu. Rev. Condens. Matter Phys.* **3**, 35 (2012).
- [11] J. Sheng, L. Wang, W. Jiang, H. Ge, N. Zhao, T. Li, M. Kofu, D. Yu, W. Zhu, J.-W. Mei *et al.*, Continuum of spin excitations in an ordered magnet, *The Innovation* **6**, 100769 (2025).
- [12] J. Sheng, L. Wang, A. Candini, W. Jiang, L. Huang, B. Xi, J. Zhao, H. Ge, N. Zhao, Y. Fu *et al.*, Two-dimensional quantum universality in the spin-1/2 triangular-lattice quantum antiferromagnet Na₂BaCo(PO₄)₂, *Proc. Natl. Acad. Sci. USA* **119**, e2211193119 (2022).
- [13] J. R. Chamorro, T. M. McQueen, and T. T. Tran, Chemistry of quantum spin liquids, *Chem. Rev.* **121**, 2898 (2021).
- [14] J. Xiang, C. Zhang, Y. Gao, W. Schmidt, K. Schmalzl, C.-W. Wang, B. Li, N. Xi, X.-Y. Liu, H. Jin *et al.*, Giant magnetocaloric effect in spin supersolid candidate Na₂BaCo(PO₄)₂, *Nature (London)* **625**, 270 (2024).
- [15] X.-Y. Liu, Y. Gao, H. Li, W. Jin, J. Xiang, H. Jin, Z. Chen, W. Li, and G. Su, Quantum spin liquid candidate as superior refrigerant in cascade demagnetization cooling, *Commun. Phys.* **5**, 233 (2022).
- [16] Y. Gao, Y.-C. Fan, H. Li, F. Yang, X.-T. Zeng, X.-L. Sheng, R. Zhong, Y. Qi, Y. Wan, and W. Li, Spin supersolidity in nearly ideal easy-axis triangular quantum antiferromagnet Na₂BaCo(PO₄)₂, *npj Quantum Mater.* **7**, 89 (2022).
- [17] N. Li, Q. Huang, X. Yue, W. Chu, Q. Chen, E. Choi, X. Zhao, H. Zhou, and X. Sun, Possible itinerant excitations and quantum spin state transitions in the effective spin-1/2 triangular-lattice antiferromagnet Na₂BaCo(PO₄)₂, *Nat. Commun.* **11**, 4216 (2020).
- [18] S. Lee, C. H. Lee, A. Berlie, A. D. Hillier, D. T. Adroja, R. Zhong, R. J. Cava, Z. H. Jang, and K.-Y. Choi, Temporal and field evolution of spin excitations in the disorder-free triangular antiferromagnet Na₂BaCo(PO₄)₂, *Phys. Rev. B* **103**, 024413 (2021).
- [19] T. V. Brinzari, J. T. Haraldsen, P. Chen, Q. C. Sun, Y. Kim, L. C. Tung, A. Litvinchuk, J. A. Schlueter, D. Smirnov, J. L. Manson *et al.*, Electron-phonon and magnetoelastic interactions in ferromagnetic Co[N(CN)₂]₂, *Phys. Rev. Lett.* **111**, 047202 (2013).
- [20] D. Lujan, J. Choe, S. Chaudhary, G. Ye, C. Nnokwe, M. Rodriguez-Vega, J. He, F. Y. Gao, T. N. Nunley, E. Baldini *et al.*, Spin-orbit exciton-induced phonon chirality in a quantum magnet, *Proc. Natl. Acad. Sci. USA* **121**, e2304360121 (2024).
- [21] S. Mukherjee, N. Mondal, M. Polentarutti, G. Bais, S. Majumdar, and S. Giri, Linear magnetoelectric coupling without long-range magnetic order and rare-earth-free large magnetocaloric effect in Co₃V₂O₈, *Phys. Rev. B* **109**, 014418 (2024).
- [22] M. Sorolla II, X. Wang, H.-J. Koo, M.-H. Whangbo, and A. J. Jacobson, Synthesis of the elusive $S = 1/2$ star structure: A possible quantum spin liquid candidate, *J. Am. Chem. Soc.* **142**, 5013 (2020).
- [23] Y. Hinuma, G. Pizzi, Y. Kumagai, F. Oba, and I. Tanaka, Band structure diagram paths based on crystallography, *Comput. Mater. Sci.* **128**, 140 (2017).
- [24] J. P. Perdew, K. Burke, and M. Ernzerhof, Generalized gradient approximation made simple, *Phys. Rev. Lett.* **77**, 3865 (1996).
- [25] B. S. Mou, X. Zhang, L. Xiang, Y. Xu, R. Zhong, R. J. Cava, H. Zhou, Z. Jiang, D. Smirnov, N. Drichko *et al.*,

- Comparative Raman scattering study of crystal field excitations in Co-based quantum magnets, *Phys. Rev. Mater.* **8**, 084408 (2024).
- [26] F. Soyalt, M. Yavuz, and Z. Yalçın, *Ab initio* investigations of phonons and thermodynamic properties of ScZn and YZn in the B₂ structure, *Comput. Mater. Sci.* **77**, 72 (2013).
- [27] Y. Ye, M. Weng, W. Zhang, W. Lin, T. Chen, F. Pan, J. Zheng, and L.-W. Wang, Calculating electron-phonon coupling matrix: Theory introduction, code development and preliminary application, *Sci. China Technol. Sci.* **66**, 204 (2023).
- [28] A. Abragam and B. Bleaney, *Electron Paramagnetic Resonance of Transition Ions* (Oxford University Press, Oxford, UK, 2012).
- [29] See Supplemental Material at <http://link.aps.org/supplemental/10.1103/PhysRevB.111.155129> for additional Raman spectra.
- [30] X. Zhang, Q.-H. Tan, J.-B. Wu, W. Shi, and P.-H. Tan, Review on the Raman spectroscopy of different types of layered materials, *Nanoscale* **8**, 6435 (2016).
- [31] S. Mashhadi, D. Weber, L. M. Schoop, A. Schulz, B. V. Lotsch, M. Burghard, and K. Kern, Electrical transport signature of the magnetic fluctuation-structure relation in α -RuCl₃ nanoflakes, *Nano Lett.* **18**, 3203 (2018).
- [32] T. Y. Kim and C.-H. Park, Magnetic anisotropy and magnetic ordering of transition-metal phosphorus trisulfides, *Nano Lett.* **21**, 10114 (2021).
- [33] R. S. Alencar, R. Longuinhos, C. Rabelo, H. Miranda, B. C. Viana, A. G. S. Filho, L. Caçado, A. Jorio, and J. Ribeiro-Souares, Raman spectroscopy polarization dependence analysis in two-dimensional gallium sulfide, *Phys. Rev. B* **102**, 165307 (2020).
- [34] M. V. Klein, Raman studies of phonon anomalies in transition-metal compounds, in *Light Scattering in Solids III*, edited by M. Cardona and G. Güntherodt (Springer, Berlin, 1982), pp. 128–178.
- [35] S. Zhang, X. Yang, B. L. Wooten, R. Bag, L. Yadav, C. E. Moore, S. Parida, N. Trivedi, Y. Lu, J. P. Heremans *et al.*, Two-dimensional cobalt(II) benzoquinone frameworks for putative Kitaev quantum spin liquid candidates, *J. Am. Chem. Soc.* **146**, 15061 (2024).
- [36] A. Scheie, PYCRYSTALFIELD: Software for calculation, analysis and fitting of crystal electric field Hamiltonians, *J. Appl. Crystallogr.* **54**, 356 (2021).
- [37] C. Wellm, W. Roscher, J. Zeisner, A. Alfonsov, R. Zhong, R. J. Cava, A. Savoyant, R. Hayn, J. van den Brink, B. Büchner *et al.*, Frustration enhanced by Kitaev exchange in a $\tilde{j}_{\text{eff}} = \frac{1}{2}$ triangular antiferromagnet, *Phys. Rev. B* **104**, L100420 (2021).
- [38] S. M. Winter, Magnetic couplings in edge-sharing high-spin d⁷ compounds, *J. Phys. Mater.* **5**, 045003 (2022).
- [39] M. Lee, D. Sheng, and S.-P. Lim, Spin-liquid and quantum phase diagram on a spin-orbit coupled triangular lattice, Ph.D. thesis, California State University, Northridge, 2018.
- [40] K. Nakamoto, *Infrared and Raman Spectra of Inorganic and Coordination Compounds, Part B: Applications in Coordination, Organometallic, and Bioinorganic Chemistry* (Wiley, Hoboken, NJ, 2009).
- [41] K.-S. Lee, J.-H. Ko, J. Moon, S. Lee, and M. Jeon, Raman spectroscopic study of LiH₂PO₄, *Solid State Commun.* **145**, 487 (2008).
- [42] S. Zhai, A. Liu, W. Xue, and Y. Song, High-pressure Raman spectroscopic studies on orthophosphates Ba₃(PO₄)₂ and Sr₃(PO₄)₂, *Solid State Commun.* **151**, 276 (2011).
- [43] Y. Liu, Q. Ai, G. Ye, Z. Ye, J. Hrubý, F. Wang, T. Orlando, Y. Wang, J. Luo, Q. Fang *et al.*, Spin-phonon coupling in iron-doped ultrathin bismuth halide perovskite derivatives, *ACS Nano* **18**, 12560 (2024).
- [44] C. N. R. Rao, Transition metal oxides, *Annu. Rev. Phys. Chem.* **40**, 291 (1989).
- [45] A. Sethi, J. E. Slimak, T. Kolodiazny, and S. L. Cooper, Emergent vibronic excitations in the magnetodielectric regime of Ce₂O₃, *Phys. Rev. Lett.* **122**, 177601 (2019).
- [46] J. E. Slimak, A. Cote, G. MacDougall, and S. L. Cooper, Soft-phonon anomalies and crystal electric field-phonon coupling in cubic lanthanide sesquioxides Eu₂O₃ and Yb₂O₃, *Phys. Rev. B* **108**, 045128 (2023).
- [47] J. E. Slimak, A. Sethi, T. Kolodiazny, and S. L. Cooper, Soft mode behavior and evidence for pressure-induced magnetostructural effects in Pr₂O₃, *Phys. Rev. Res.* **2**, 043169 (2020).
- [48] C. Kim, J. Jeong, G. Lin, P. Park, T. Masuda, S. Asai, S. Itoh, H.-S. Kim, H. Zhou, J. Ma *et al.*, Antiferromagnetic Kitaev interaction in $j_{\text{eff}} = 1/2$ cobalt honeycomb materials Na₃Co₂SbO₆ and Na₂Co₂TeO₆, *J. Phys.: Condens. Matter* **34**, 045802 (2022).
- [49] C. H. Lee, S. Lee, Y. S. Choi, Z. H. Jang, R. Kalaivanan, R. Sankar, and K.-Y. Choi, Multistage development of anisotropic magnetic correlations in the Co-based honeycomb lattice Na₂Co₂TeO₆, *Phys. Rev. B* **103**, 214447 (2021).
- [50] L. Y. Shi, X. M. Wang, R. D. Zhong, Z. X. Wang, T. C. Hu, S. J. Zhang, Q. M. Liu, T. Dong, F. Wang, and N. L. Wang, Magnetic excitations of the field-induced states in BaCo₂(AsO₄)₂ probed by time-domain terahertz spectroscopy, *Phys. Rev. B* **104**, 144408 (2021).
- [51] C. Kim, S. Kim, P. Park, T. Kim, J. Jeong, S. Ohira-Kawamura, N. Murai, K. Nakajima, A. Chernyshev, M. Mourigal *et al.*, Bond-dependent anisotropy and magnon decay in cobalt-based Kitaev triangular antiferromagnet, *Nat. Phys.* **19**, 1624 (2023).
- [52] S. Chaudhary, D. M. Juraschek, M. Rodriguez-Vega, and G. A. Fiete, Giant effective magnetic moments of chiral phonons from orbit-lattice coupling, *Phys. Rev. B* **110**, 094401 (2024).
- [53] Y. Ren, C. Xiao, D. Saporov, and Q. Niu, Phonon magnetic moment from electronic topological magnetization, *Phys. Rev. Lett.* **127**, 186403 (2021).
- [54] P. Thalmeier and P. Fulde, Bound state between a crystal-field excitation and a phonon in CeAl₂, *Phys. Rev. Lett.* **49**, 1588 (1982).
- [55] P. Thalmeier, Theory of the bound state between phonons and a CEF excitation in CeAl₂, *J. Phys. C* **17**, 4153 (1984).
- [56] S. L. Altmann and P. Herzig, *Point-group Theory Tables* (Clarendon Press and Oxford University Press, 1994).
- [57] J. E. Slimak, II, CEF-phonon interactions in rare earth sesquioxides: Pressure-, temperature-, and magnetic field-dependent Raman scattering studies, Ph.D. thesis, University of Illinois at Urbana-Champaign, 2024.